Experimental dynamical encircling of an exceptional point in coupled pendulums

Nicolas Even, Benoit Nennig, Gautier Lefebvre, Emmanuel Perrey-Debain

PROCEEDINGS A

rspa.royalsocietypublishing.org

Research

Article submitted to journal

Keywords:
exceptional point, encirlcing, mode switching, chirality, non-hermitian, time varying parameters

Author for correspondence:
B. Nennig
e-mail:
benoit.nennig@isae-supmeca.fr

Experimental dynamical encircling of an exceptional point in coupled pendulums

Nicolas Even[1,2], Benoit Nennig[1], Gautier Lefebvre[2], Emmanuel Perrey-Debain[2]

[1]Institut supérieur de mécanique de Paris (ISAE-SUPMECA) - Laboratoire Quartz EA 7393
3 rue Fernand Hainaut, 93407 Saint-Ouen, France
[2]Université de technologie de Compiègne, Roberval (Mechanics, energy and electricity)
Centre de recherche Royallieu
CS 60319 - 60203 Compiègne Cedex - France

Exceptional points (EPs) correspond to specific values of the system parameters that yield defective eigenvalues.
The concept is demonstrated experimentally in the case of a simple mechanical system consisting of two coupled linearized pendulums. The latter is designed and instrumented in order to allow the encircling of an EP: the modulation of both the mass and stiffness matrices is achieved by controlling the length of one pendulum whereas the damping is controlled by using eddy current brake mechanisms. The time evolution of the state vector, identified with the help of the extended Kalman filter, is described using the instantaneous modal basis. This allows one to quantify and observe mode coupling mechanisms, non-adiabatic effects and chiral behavior. The paper ends with a numerical study, via the analysis of the monodromy matrix and the multiple-scale approach, which illustrates both the effect on chirality of the period of encircling as well as the presence of an EP in the loop.

THE ROYAL SOCIETY PUBLISHING

Accepted version. Build by the authors from 'rsproca_new' class.

1. Introduction

Exceptional points (EPs) are special degeneracies corresponding to specific values of the system parameters for which both eigenfrequencies and eigenmodes coalesce simultaneously [1]. Their existence is well documented in the context of non-Hermitian systems, arising notably in the field of quantum physics, optics and photonics [2–4] and especially in PT-symmetric systems [5]. In the vicinity of an EP, perturbation analysis in the parametric space shows that some eigenvalues exhibit a branch point singularity giving rise to a self-intersecting Riemann topological structure of the eigenvalue surface.

The idea of encircling an EP [6] is born in this context: if the system parameters are modified sufficiently slowly it becomes possible to switch the system's state from one mode to the other by exploiting the fact that their eigenvalue surface are both connected at the EP (this can not be observed when encircling a diabolical point [7], which is a Hermitian degeneracy).

Adiabatic encircling experiments, i.e. in the quasi-static limit, were conducted for scattering in a microwave cavity [8]. In these experiments, the resonators coupling and damping are changed while steady excitation can be maintained. The expected flip of eigenvalues and eigenvectors and the sign change of one of the eigenvectors was observed. Similar results were also obtained later using exciton-polariton systems [9]. Later theoretical works [10–13] show that even for arbitrary slow encircling, non-adiabatic effects never totally vanish and this limits the possibility to achieve modal flip for both eigenstates. Generally, only the least-damped mode follows adiabatic prediction [10].

The system response behaves differently when a dynamical encirclement is performed. After encircling the EP, the system response can exhibit chiral transformations as shown in [6,10], whereby the output is solely determined by the encircling direction, regardless of the initial state. Various approaches can be followed to explain this behavior, we can cite the Stokes' phenomenon [11], the stability loss delay arising with singular perturbation theory [13] or by using the concept of Floquet EPs for repeated encirclements [14,15]. The latter corresponds to an exceptional point of the monodromy matrix [16, chap. 5] and this is known to delimit the stability region of parametric oscillators [15].

Experimental evidences of the chirality have been proposed first by Doppler et al. [17] using a spatial modulation of a microwave waveguide to encircle an EP connecting two transverse modes. Similar research have been conducted in [18,19]. A growing number of experiments have been reported in various branches of physics. We can cite for instance the study of cryogenic optomechanical systems [20], photonics devices [21–23] or the interaction between light and an organic molecule [24]. Encirclement of two exceptional points is considered in [19].

The consideration of EPs in dynamical systems has also been motivated by the potential practical applications in energy transport [20], asymmetric mode switching [17,25] or polarization control of light [26] required by advanced signal processing systems in telecommunications. Other applications can be found in duct acoustics (although no encircling is reported), where EPs are strongly connected to optimal wave attenuation [27–29].

Recent numerical and experimental studies have shown that chirality conditions are still not fully understood and do not depend solely on the encircling speed. For instance, Zhang et al. [18] have experimentally shown that the chiral behavior also depends on the starting point and in order to observe chiral behavior, the two modes should initially suffer from similar losses. The encirclement shape in the parametric space is also of primary interest, since the final states after two distinct homotopic encircling may be completely different [30]. This has led some authors to optimize the contour in order to maximize the chirality [23].

In [31,32], chiral conversion is obtained in the vicinity of the EP but without encircling it. Similar observations are reported in [15] where a Möebius group classification is proposed to explain the origin of this behavior. For periodic encirclements, Longhi [14] provides the condition to reach chirality using the concept of Floquet EP. These examples show that dynamical

encirclements, as opposed to adiabatic, yields modal conversions which depend strongly on the encirclement period and are harder to anticipate.

If experimental evidences of EP (including encirclements) have been reported in many areas of physics, applications to mechanical systems seems to be missing in the scientific literature. One can cite a recent numerical work in acoustics where the time-evolution scenario is replaced by the design of spatially coupled acoustic systems [33]. In [34], the authors propose a two-mode mass–spring–dashpot mechanical system with dynamic modulations of the stiffness and damping but no experimental data are reported. The aim of this paper is to propose an experimental platform, based on the free response of two coupled pendulums. The mechanical system, which was originally set up in its static configuration, i.e. where parameters are time-invariant [35], has been designed and instrumented in order to allow the encircling of an EP with the aim of illustrating chirality and asymmetric mode swapping. Here, the modulation of both the mass and stiffness matrices is achieved by controlling the length of one pendulum whereas the damping is controlled by using eddy current brake mechanisms. The experimental set-up and the governing equations are presented in Sec. 2. The observation of the dynamical system is described via its modal description using the instantaneous modal basis (see Sec. 3) and this requires the precise knowledge of the time evolution of the state vector. Here, a full temporal analysis of the free response is proposed with the help of the extended Kalman filter (EKF) [36]. This tool simplifies signal processing especially when eigenfrequencies are nearly coalescing and this is explained in Sec. 4. The time evolution of the modal coefficients, either measured experimentally or calculated, allows us to quantify and observe mode coupling mechanisms, non-adiabatic effects and chiral behavior and this is the subject of Sec. 5. Finally, a numerical study is presented in Sec. 6, illustrating both the effect on chirality of the period of encircling as well as the presence of an EP in the loop.

2. Experimental set-up and governing equations

The experimental set-up, based on 3B Scientific (No. 8000563 UE1050600-230), consists of two pendulums coupled by a spring as shown in Fig. 1a). Each pendulum consists of a bob of mass m_s ($s=1$ or $s=2$) fixed at a distance L_s from the pivot and coupled by a spring of stiffness k fixed at a distance d from each pivot, as shown in Fig. 1b). The angles θ_i of each pendulum were measured thanks to Hall-effect sensors. These sensors convert the angle into a proportional voltage, which is recorded at 50 Hz by the NI-9223 voltage input module (No. 783284-01).

The encirclement is carried out by using an experimental set-up with two controllable parameters. The bob of the second pendulum is moved by an electric linear actuator (Actuonix) which speed is directly proportional to the voltage applied to it. A magnetic device was designed to obtain a controllable and viscous damping of the second pendulum. This is achieved by means of an aluminum plate fixed at the end of the rod of the second pendulum and oscillating in a magnetic field generated by two solenoids. The resulting eddy currents are responsible for a damping proportional to the square of the current I. Following the calibration procedure [35], the magnetic damping follows the quadratic law

$$c_2(I) \approx 0.71 I^2 + 8.9 \cdot 10^{-3}. \tag{2.1}$$

The equations of motion for the generalized coordinates vector $\mathbf{q} = [\theta_1, \theta_2]^{\mathrm{T}}$ can be written in matrix form

$$\mathbf{M}(t)\ddot{\mathbf{q}} + \mathbf{C}(t)\dot{\mathbf{q}} + \mathbf{K}(t)\mathbf{q} = \mathbf{0}, \tag{2.2}$$

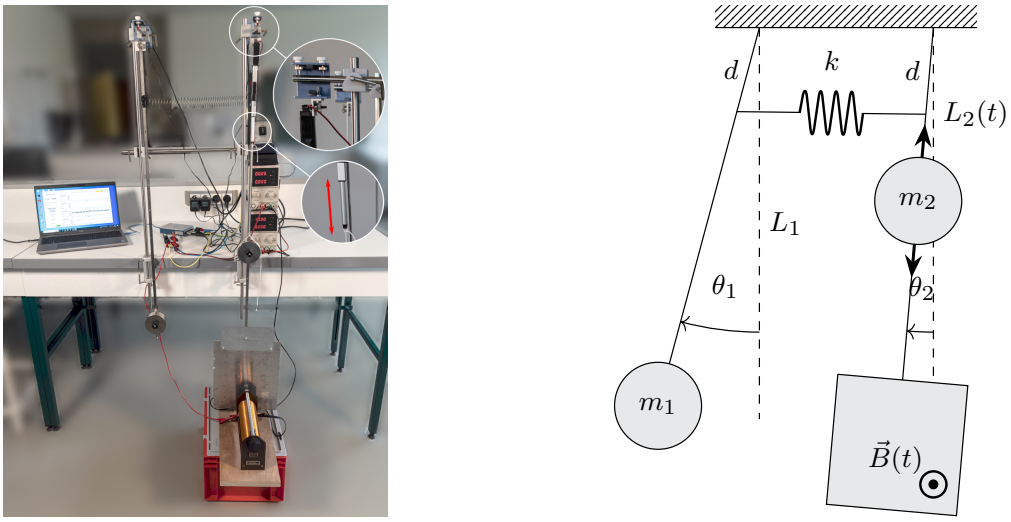

(a) (b)

Figure 1. Experimental set-up (a) and sketch of the coupled pendulums (b).

with

$$\mathbf{M}(t) = \begin{bmatrix} m_1 L_1^2 + I_1 & 0 \\ 0 & m_2 L_2^2(t) + I_2 \end{bmatrix}, \tag{2.3}$$

$$\mathbf{C}(t) = \begin{bmatrix} c_1 + c_{12} & -c_{12} \\ -c_{12} & c_2(t) + c_{12} \end{bmatrix}, \tag{2.4}$$

$$\mathbf{K}(t) = \begin{bmatrix} m_1 g L_1 + \Omega_1^2 I_1 + k_{12} & -k_{12} \\ -k_{12} & m_2 g L_2(t) + \Omega_2^2 I_2 + k_{12} \end{bmatrix}. \tag{2.5}$$

Here $k_{12} = kd^2$, where the subscript 12 refers to the coupling term. The presence of the conductive plate must also be considered in our model. To do so, its inertia and natural angular frequencies, including the plate and the rod (except the bob), are grouped in I_s and Ω_s (s=1 or 2). See Eq. (2) in [35] for more details. Although negligible due to the nearly frictionless pivot points, we also include the damping coefficients c_1 and c_{12}, which represent the residual damping of the first pendulum due to the air drag and the relative motion between the pendulums, respectively.

It is more convenient to recast Eq. (2.2) in its state-space form

$$\mathbf{A}(t)\mathbf{p} = \mathbf{B}(t)\dot{\mathbf{p}}, \tag{2.6}$$

using the first companion form [37]

$$\mathbf{A}(t) = \begin{bmatrix} \mathbf{0} & \mathbf{I} \\ -\mathbf{K}(t) & -\mathbf{C}(t) \end{bmatrix}, \qquad \mathbf{B}(t) = \begin{bmatrix} \mathbf{I} & \mathbf{0} \\ \mathbf{0} & \mathbf{M}(t) \end{bmatrix}, \tag{2.7}$$

where $\mathbf{p} = [\theta_1, \theta_2, \dot{\theta}_1, \dot{\theta}_2]^{\mathrm{T}}$. The constant parameters of our model, which have been identified in [35], are reported in Table 1 (note some values may be slightly different from [35] due to mounting and unmounting of the experimental set-up).

Table 1. Parameters of the dynamical system. The identification procedure is explained in [35]. In bold are the specific values of the controllable parameters (L_2, c_2) at the EP, retrieved from the search algorithm in [35] (See also https://github.com/nicolase7en/real-valued-ep2).

s	m_s (kg)	I_s (kg m^2)	Ω_s (rad s^{-1})	L_s (m)	c_s (N m s)	k_s (N m)
1	1	0.055	3.782	0.953	$\sim 10^{-3}$	
2	1	1.015	2.964	**0.671**	**0.123**	
12					$\sim 10^{-4}$	0.160

3. Theoretical considerations

(a) Time-dependent modal analysis

Following the coupled mode theory, largely employed in electromagnetics [38], the time dependent system (2.6) is amenable to a mode description using the instantaneous modes $\mathbf{x}_i(t)$ satisfying

$$\mathbf{A}(t)\mathbf{x}_i(t) = \lambda_i(t)\mathbf{B}(t)\mathbf{x}_i(t). \tag{3.1}$$

This is completed by the bi-orthogonal basis consisting of the left eigenvectors $\mathbf{y}_j(t)$ which are normalized so that

$$\mathbf{y}_j^{\mathrm{H}}(t)\mathbf{B}(t)\mathbf{x}_i(t) = \delta_{ij}. \tag{3.2}$$

As complex eigenmodes and eigenvalues occur in conjugate pairs [1], the modal expansion reads

$$\begin{aligned}\mathbf{p}(t) &= \sum_{i=1}^{4} a_i(t)\mathbf{x}_i(t) \\ &= 2\,\mathrm{Re}(a_1(t)\mathbf{x}_1(t) + a_2(t)\mathbf{x}_2(t)).\end{aligned} \tag{3.3}$$

Straightforward application of the orthogonality properties leads to a system of two linear coupled ODEs

$$\dot{a}_i = \left(\lambda_i - \mathbf{y}_i^{\mathrm{H}}\mathbf{B}\dot{\mathbf{x}}_i\right)a_i - \mathbf{y}_i^{\mathrm{H}}\mathbf{B}\dot{\mathbf{x}}_j a_j, \quad j \neq i. \tag{3.4}$$

The system involves the time derivative of the eigenvectors $\mathbf{x}_i$ which can be found by solving the bordered matrix [39]

$$\begin{bmatrix}\mathbf{A} - \lambda_i\mathbf{B} & -\mathbf{B}\mathbf{x}_i \\ \mathbf{n}^{\mathrm{T}} & 0\end{bmatrix}\begin{bmatrix}\dot{\mathbf{x}}_i \\ \dot{\lambda}_i\end{bmatrix} = \begin{bmatrix}-\left(\dot{\mathbf{A}} - \lambda_i\dot{\mathbf{B}}\right)\mathbf{x}_i \\ 0\end{bmatrix}, \tag{3.5}$$

where $\mathbf{n}$ is a constant vector which serves to impose the normalization of the right eigenvectors

$$\mathbf{n}^{\mathrm{T}}\mathbf{x}_i(t) = 1. \tag{3.6}$$

Here, $\mathbf{n}$ must be chosen on the condition that it is not orthogonal to the eigenvector basis and its exact definition will be clarified later. The time derivative of the right-hand side is calculated via

[1] This is true except when eigenvalues are real-valued but this situation is not considered here.

the chain rule

$$\dot{\mathbf{A}} = \dot{c_2}\partial_{c_2}\mathbf{A} + \dot{L_2}\partial_{L_2}\mathbf{A} \quad \text{and} \quad \dot{\mathbf{B}} = \dot{L_2}\partial_{L_2}\mathbf{B}. \tag{3.7}$$

Now, neglecting the coupling terms in Eq. (3.4) leads to the well known adiabatic solution which has the exact exponential form

$$a_i^{\text{ad.}}(t) = \mathrm{e}^{\mathrm{i}\gamma_i(t)}a_i(0), \quad \gamma_i = \gamma_i^{\text{d}} + \gamma_i^{\text{g}}, \tag{3.8}$$

with the dynamical phase

$$\gamma_i^{\text{d}}(t) = -\mathrm{i}\int_0^t \lambda_i(\tau)\,\mathrm{d}\tau, \tag{3.9}$$

and the geometric phase [7,40]

$$\gamma_i^{\text{g}}(t) = \mathrm{i}\int_0^t \mathbf{y}_i^{\text{H}}(\tau)\mathbf{B}(\tau)\dot{\mathbf{x}}_i(\tau)\,\mathrm{d}\tau. \tag{3.10}$$

Though there is no closed-form solution for the coupled system (3.4), we can assume that parameters of the problem are sufficiently slowly-varying and show that the first order correction term in the Magnus expansion:

$$a_i^{\text{cor.}}(t) = -\mathrm{e}^{\mathrm{i}\gamma_i(t)}\Gamma_{ij}(t)a_j(0), \text{ with } i \neq j \tag{3.11}$$

with

$$\Gamma_{ij}(t) = \int_0^t \mathbf{y}_i^{\text{H}}(\tau)\mathbf{B}(\tau)\dot{\mathbf{x}}_j(\tau)\mathrm{e}^{\mathrm{i}(\gamma_j(\tau)-\gamma_i(\tau))}\,\mathrm{d}\tau, \tag{3.12}$$

should provide a good estimate and

$$a_i(t) \approx a_i^{\text{ad.}}(t) + a_i^{\text{cor.}}(t). \tag{3.13}$$

(b) Encirclement of an exceptional point

The above analysis is valid except if the algebraic system (3.1) is defective for a specific choice of the controllable parameters. This happens here if

$$\partial_\lambda D(\lambda_0, c_2^0, L_2^0) = 0 \tag{3.14}$$

where $D(\lambda, c_2, L_2) = \det(\mathbf{A} - \lambda\mathbf{B})$ is the characteristic polynomial. Note that matrices must be regarded as functions of the controllable parameters, i.e. $\mathbf{A}(L_2, c_2)$ and $\mathbf{B}(L_2)$. Here, the pair (c_2^0, L_2^0) defines an exceptional point (EP) associated with the double root λ_0. The location of EP in the context of our experimental set-up has been the subject of a recent paper [35] and, for the sake of completeness, the values of controllable parameters at the EP (c_2^0, L_2^0) are reported in Table 1.

The condition (3.14) means that, in the vicinity of an EP, eigenvalues exhibit a branch point singularity [1]:

$$\lambda_i \approx \lambda_0 + (-1)^i\sqrt{\Delta} \tag{3.15}$$

where

$$\Delta = -2\frac{(c_2 - c_2^0)\partial_{c_2}D + (L_2 - L_2^0)\partial_{L_2}D}{\partial_\lambda^2 D} \tag{3.16}$$

and all derivatives are evaluated at EP. The same analysis also holds for the eigenmodes and

$$\mathbf{x}_i \approx \mathbf{x}_0 + (-1)^i\sqrt{\Delta}\,\tilde{\mathbf{x}}_0. \tag{3.17}$$

where $\mathbf{x}_0$ is the unique eigenvector associated with the double root λ_0 and $\tilde{\mathbf{x}}_0$ is the generalized eigenvector. Encircling an EP signifies that controllable parameters are T-periodic functions such that $\Delta(t)$ must define a closed loop in the complex plane around the origin. After a single

loop, the expected swapping of eigenvalues (and eigenvectors), follows from the topology of the eigenvalue spectrum illustrated by the square root singularity in (3.15). In other words,

$$\mathbf{x}_i(0) = \mathbf{x}_j(T) = \mathbf{x}_i(2T), \quad i \neq j. \tag{3.18}$$

This point is best illustrated in the scenario where the system is initially conservative so we have $c_2(0) = 0$ (damping coefficients c_1 and c_{12} can be neglected). The two vibrational modes are then real-valued and orthogonal, and can be classified as 'in-phase' (IP) and 'out-of phase' (OP). At $t = T$, modal coefficients $a_{i=1,2}$, which are initially associated with IP/OP modes, become associated with OP/IP modes.

4. Signal processing and validation of the theoretical model

An experimental observation of the dynamical system via its modal description requires the precise knowledge of the time evolution of the state vector $\mathbf{p}$ and of the matrix operators $\mathbf{A}$ and $\mathbf{B}$. The encirclement of an EP signifies that the pair of time-dependent eigenvalues $\lambda_i(t)$ are expected to remain nearly identical (see Eq. (3.15)) and the use of standard short term Fourier transforms or other high resolution methods like ESPRIT [41] is not appropriate to track modal coordinates. Improvements can be made thanks to a hybrid approach that exploits both the dynamical modeling and experimental data by using the Extended Kalman Filter (EKF) [36].

(a) Extended Kalman filter

The Kalman filter (KF) is a recursive mathematical algorithm used to estimate the state of the system from a series of measurements, providing optimal identification by combining predictions and measurements while minimizing error variance for a linear system subject to white noise. In the present case, the extended state system contains all the time-dependent variables and their first derivatives:

$$\mathbf{s} = [\theta_1, \dot{\theta}_1, \theta_2, \dot{\theta}_2, L_2, \dot{L}_2, c_2, \dot{c}_2]^{\mathrm{T}}.$$

The EKF allows us to address the non-linearity of the response with respect to the pendulum length $L_2(t)$ and the damping modulation $c_2(t)$. The main algorithmic steps are indicated in Table. 2. Note that although the EKF is now a well-established procedure, some useful details which are associated with our experiment are reminded below.

Table 2. Algorithm of the EKF used here, where $\mathbf{F}_k = \frac{\partial \mathbf{f}}{\partial \mathbf{s}}\big|_{\hat{\mathbf{s}}_{k-1|k-1}}$ is the Jacobian matrix (the notation $k|j$ signifies that the variable is estimated at time-step k given observations up to time-step j).

Extended Kalman filter
Predict with the model
$\hat{\mathbf{s}}_{k\|k-1} = \mathbf{f}(\mathbf{s}_{k-1\|k-1})$
$\hat{\mathbf{P}}_{k\|k-1} = \mathbf{F}_k \mathbf{P}_{k-1\|k-1} \mathbf{F}_k^{\mathrm{T}} + \mathbf{Q}_k$
Update with the experiment
$\tilde{\mathbf{y}}_k = \mathbf{z}_k - \mathbf{H}\hat{\mathbf{s}}_{k\|k-1}$
$\mathbf{S}_k = \mathbf{H}_k \hat{\mathbf{P}}_{k\|k-1} \mathbf{H}_k^{\mathrm{T}} + \mathbf{R}_k$
$\mathbf{K}_k = \hat{\mathbf{P}}_{k\|k-1} \mathbf{H}_k^{\mathrm{T}} \mathbf{S}_k^{-1}$
$\mathbf{s}_{k\|k} = \hat{\mathbf{s}}_{k\|k-1} + \mathbf{K}_k \tilde{\mathbf{y}}_k$
$\mathbf{P}_{k\|k} = (\mathbf{I} - \mathbf{K}_k \mathbf{H}_k) \hat{\mathbf{P}}_{k\|k-1}$

First, a prediction $\hat{\mathbf{s}}$ of the state is made using the state transition function $\mathbf{f}$ applied to the previous estimate $\mathbf{s}$. This function is obtained by solving the differential equations using classic Runge–Kutta method (RK4) until the next measurement. Here, the equations of motion (2.6)

are combined with the evolution equations for $c_2(t)$ and $L_2(t)$ assuming a constant acceleration model [36].

A prediction $\hat{\mathbf{P}}$ of the covariance matrix is made as well. Then, a new measurement $\mathbf{z}$ is taken into account to compute the measurement residual $\tilde{\mathbf{y}}$. However, because all the state variable may not be observed, the linear observation model $\mathbf{H}$ is used to map the true state space into the observed space. The residual covariance $\mathbf{S}$ is also computed. Using both covariance matrices, the Kalman gain $\mathbf{K}$ is computed. Basically, it indicates how much the measure should impact the state estimate $\mathbf{s}$ and covariance estimate $\mathbf{P}$ based on the two covariance matrices.

The difficult part of KF relies on the initialization of the error covariance matrix $\mathbf{P}$, the process noise covariance matrix $\mathbf{Q}$ and the measurement noise covariance matrix $\mathbf{R}$, where the latter two are assumed to be diagonal and constant. The variance of the matrices $\mathbf{P}$, $\mathbf{Q}$ and $\mathbf{R}$ are initialized at 0.1, 0.01 and 0.01, respectively. These values were based on an upper bound of the measurements and numerical error and after some preliminary tests.

We consider for the moment that we only observe the angles of each pendulum (in this case, the observation model is linear and simply given by the diagonal matrix $\mathbf{H} = \mathrm{diag}(1, 0, 1, 0, 0, 0, 0, 0)$). The estimated values of $L_2(t)$ and $c_2(t)$ are shown in Fig. 2. The two signals, although noisy,

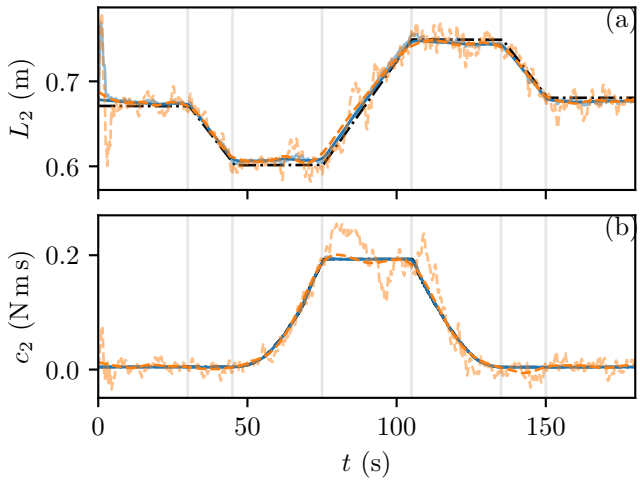

Figure 2. (color online) Estimated values of (a) L_2 and (b) c_2 with (light blue (resp. blue) solid line) or without (light orange (resp. orange) dashed line) their measure (black dash-dotted line) before (resp. after) RKS smoothing.

are in good agreement (except near the initial time since few iterations are required for the filter to converge) with the target values. It was also observed that the agreement is even better for the angular velocities and that their estimation is less sensitive to noise than if derivatives were computed numerically. Discrepancies are noticeable in the interval $75\,\mathrm{s} \leq t \leq 85\,\mathrm{s}$ where the second pendulum is nearly at rest (see Fig 3(a)) which is a consequence of a beating phenomenon. Results can be smoothed out, by using the Rauch–Tung–Striebel (RTS) smoother [36,42], which incorporate measurements from the past and the future via application of forward and backward EKF. The quality of the estimation, clearly shown in Fig. 2, validates both the EKF algorithm and the equations of motion given by the linear model (2.2).

These estimations can be further improved by upgrading the experimental set-up in order to measure both parameters L_2 and c_2. As they are controlled by electric devices, it is therefore possible to recover a tension proportional to the square of the magnetic damping, and another one proportional to the velocity of the bob along the second pendulum. In this case, the observation model $\mathbf{H} = \mathrm{diag}(1, 0, 1, 0, 0, 1, 1, 0)$. Results (in blue solid line) shown in Fig. 2 are in perfect

agreement with the target values. Note that the damping coefficient increases and decreases quadratically (in time) following Eq. (2.1).

(b) Modal coefficient retrieval

Using the EKF approach just described, all time-dependent variables, which includes the rotation angles and the controllable parameters, are shown in Fig. 3. In this example, the choice was made to encircle the EP following a rectangular shape in the parametric space (L_2, c_2), as sketched in Fig. 4. It can be observed that, although initial and final parametric values are identical, the dynamic behavior has changed after a single loop from the IP mode to the OP one. This is a clear manifestation of the switching phenomenon which was expected.

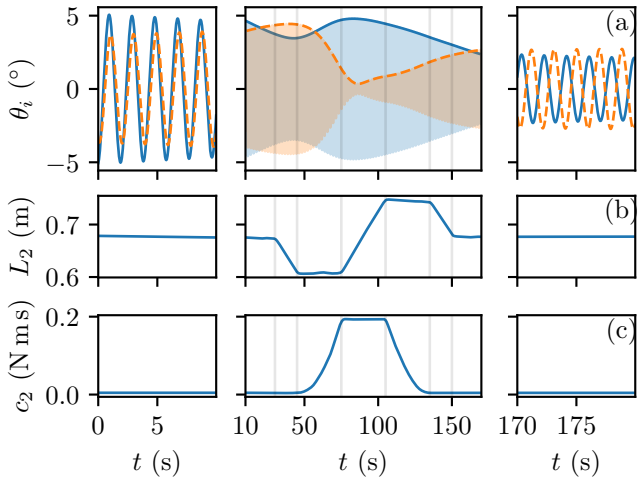

Figure 3. Triptychs of (a) the first (blue solid line) and second pendulum (orange dashed line), (b) the length L_2 and (c) the damping coefficient c_2 (both values are identified using the EKF approach). In the second figure of (a), only the envelopes of the signals are highlighted for the sake of readability.

These observations are conveniently described via the analysis of the experimental modal coefficients, which can be retrieved either by straightforward projection

$$a_i(t) = \mathbf{y}_i^{\mathrm{H}}(t)\mathbf{B}(t)\mathbf{p}(t) \tag{4.1}$$

or by solving the coupled-mode equations system (3.4). Here, the modal basis is defined via the normalization (3.6) by choosing the normalization vector as the unique eigenvector associated with the double root λ_0. Results are shown in Fig. 5(b)). Note that results obtained with the projection method exhibit a discontinuity (around $t \approx 90\,\mathrm{s}$) which is simply due to the definition of the correspondence $i \leftrightarrow \lambda_i$, which is given by ordering the imaginary part of the eigenvalues. This does not happen when eigenmodes are tracked *continuously* via Eq. (3.5). Because the mode switching IP $\leftrightarrow$ OP renders the analysis somewhat counter-intuitive, a description of the movement via projection on the initial basis (at $t = 0$), i.e.

$$\mathbf{p}(t) = 2\,\mathrm{Re}\Big(a_1^0(t)\mathbf{x}_1(0) + a_2^0(t)\mathbf{x}_2(0)\Big), \tag{4.2}$$

where

$$a_i^0(t) = \mathbf{y}_i^{\mathrm{H}}(0)\mathbf{B}(0)\mathbf{p}(t) \tag{4.3}$$

can also be used (see results in Fig. 5(a) showing the crossing of the curves as opposed to Fig. 5(b)). Here, the initial parameters are such that $(L_2(0), c_2(0)) = (L_2^0, 0)$ as sketched in Fig. 4 and this gives the IP mode $\mathbf{v}_1(0) \approx [0.72, 0.58]^{\mathrm{T}}$ and the OP mode $\mathbf{v}_2(0) \approx [0.72, -0.59]^{\mathrm{T}}$.

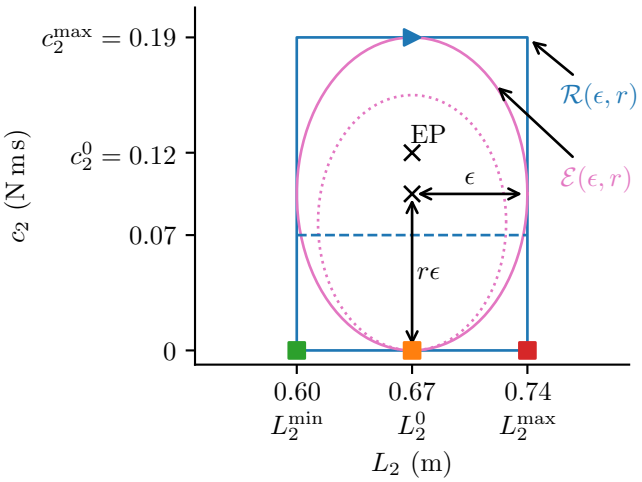

Figure 4. Encirclement contours used in the experiments (rectangular, $\mathcal{R}(\epsilon,\, r)$, blue) and in the simulations (ellipsis, $\mathcal{E}(\epsilon,\, r)$, pink). The square markers denote the starting points and the arrow indicates the CW orientation.

The evolution of the state of the system is probably best illustrated following the graphical representation taken from [13], by plotting the averaged quantity,

$$\Lambda(t) = \frac{|a_1(t)|^2\lambda_1(t) + |a_2(t)|^2\lambda_2(t)}{|a_1(t)|^2 + |a_2(t)|^2} \tag{4.4}$$

as a function of the parameters L_2 and c_2. The quantity, displayed as an orange line within Fig. 6 (c), represents the actual proportion of each mode involved in the movement at each time step, by averaging the eigenfrequencies weighed by the modal coefficients. In order to get the full picture, we also displayed the two complex eigenvalues using a Riemann surface representation, where the natural angular frequencies are plotted on the vertical axis and the value of the exponential decay constants is indicated by the color map on each surface. These results show that the EP acts as a square branch point singularity in the (L_2, c_2)-plane (although this statement is not exact from a mathematical point, since Δ can not be interpreted as a function of the complex parameter $L_2 + \mathrm{i}c_2$ [35]). A graphical representation of the bifurcation of the real and imaginary parts of the degenerate eigenvalue as a function of a parameter is also shown in Fig. 6 (a) and (b) and for the interested reader, trajectories of the two eigenvalues can be well predicted by the theory (see eq. (34) in [35]).

The trajectory of the averaged eigenvalue (4.4) clearly shows an initial dominant IP state on the bottom surface which, after one loop in the clockwise (CW) direction, becomes a dominant OP state. This is the manifestation of a quasi-adiabatic time evolution for the dominant state, as shown in Fig. 5. It is worth noting that the geometrical phase (see Fig. 5 (d)), which reflects the gain or loss in the time-dependent dynamical system, has nearly no effect on the modal amplitude after a complete loop. On the other hand, the deviation from the adiabatic prediction (also discussed in [10,13]) is evidenced by the evolution of the other state, which undergoes a non-adiabatic transition well described by the first order correction (3.11) of the coupling terms.

5. Experimental observation of chiral behavior

A transformation is said to be chiral if the dominant state, after a single loop, depends solely on the direction of encirclement. In this section, the chiral behavior is investigated experimentally. In particular, the effect of the initial state and the presence (or not) of the EP in the parametric closed curve is explored.

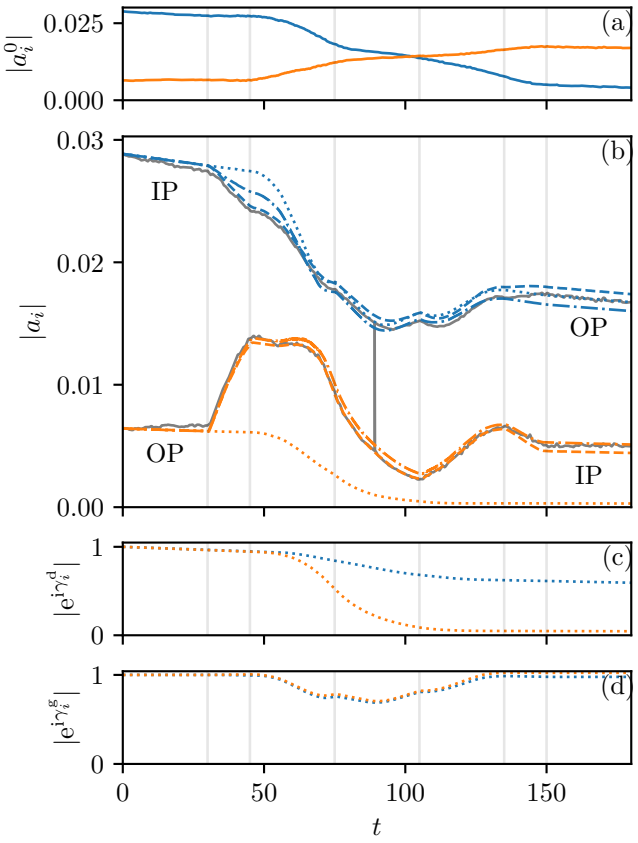

Figure 5. (color online) Modal coefficients using (a) the initial basis (b) the instantaneous basis. Dynamical (c) and geometric phase (d) during an encirclement performed between $30\,\mathrm{s}$ and $150\,\mathrm{s}$. In each case, the blue (resp. orange) line corresponds to the initial IP (resp. OP) mode. In (b) the gray solid line is computed by projection using Eq. (4.1) while the colored ones are computed by solving the coupled-mode equations. The dashed lines are obtained by solving Eq. (3.4), whereas the adiabatic prediction (3.8) is identified in dotted lines and the first order correction (3.11) in dash-dotted lines.

In Fig. 7(a-d) are shown the first (and last) ten seconds of the angular displacements of the two pendulums (note Fig. 7(a) corresponds to the experiment already presented in Sec. 4). In all cases, the initial parameters $(L_2^0, 0)$ are identical. In the clockwise (CW) encirclement, an initial dominant IP mode becomes out-of-phase due to the mode switching, as shown in Fig. 7(a). While starting with the OP mode, the system remains in this state and suffers a higher attenuation, as shown in Fig. 7(c). In the counter-clockwise (CCW) encirclement, the conclusions are similar but with the roles reversed: the IP mode remains dominant while suffering high attenuation (Fig. 7(b)) and an initial dominant OP mode eventually becomes in-phase (Fig. 7(d)).

Energy transfer between modes is given in Fig. 8 where the evolution of the modal coefficients is shown for the four scenarios. In particular, it can be seen that though the initial state is largely composed of a dominant mode (either IP or OP), the other mode is always present, this is attributed to the fact that a single mode is rather difficult to impose experimentally. In all cases, the initially dominant mode evolves nearly adiabatically whereas the modal coefficients associated with the other mode exhibit, via the coupling terms, sharp variations in response to the variations of the controllable parameters (identified by the vertical gray lines).

In order to investigate further the chiral transformation, other experiments were conducted by modifying the starting point in the parametric space. This is sketched using the Riemann surface representation in Fig. 9 where two additional starting points (without damping) are shown.

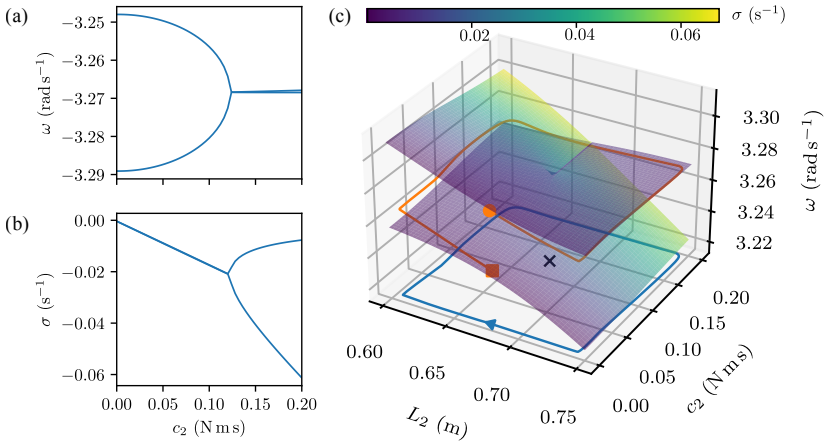

Figure 6. Trajectory of the averaged eigenvalue (in orange) using a Riemann surface representation (c): $\lambda_i = -\sigma_i + \mathrm{i}\omega_i$ $(i = 1, 2)$ as a function of (L_2, c_2), where the two natural angular frequencies ω_i, are plotted on the vertical axis and the value of the exponential decay constants σ_i is indicated by the color map on each surface. The square and circle markers indicate the initial and the final state of the system. Imaginary (a) and real part (b) of a section of the Riemann surface at $L_2 = L_2^*$ as a function of c_2.

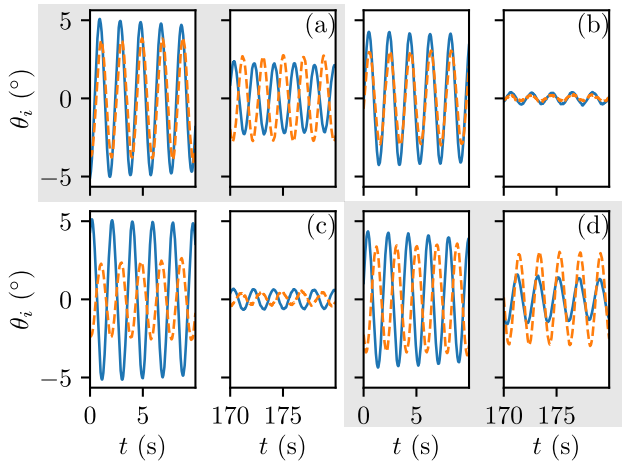

Figure 7. (color online) The first and last 10 seconds of the angular displacement for the first (blue solid line) and second pendulum (orange dashed line) with IP initially dominant state (a) CW and (b) CCW, and OP initially dominant state (c) CW and (d) CCW.

For completeness, the associated eigenvectors are $\mathbf{v}_1(0) = [0.9, 0.39]^{\mathrm{T}}$, $\mathbf{v}_2(0) = [0.47, -0.76]^{\mathrm{T}}$ for $L_2(0) = L_2^{\min}$ and $\mathbf{v}_1(0) = [0.41, 0.73]^{\mathrm{T}}$, $\mathbf{v}_2(0) = [0.93, -0.32]^{\mathrm{T}}$ for $L_2(0) = L_2^{\max}$ where it is reminded that, at $t = 0$, index $i = 1, 2$ refers to the IP and OP mode. Clearly the chiral effect is present in all cases irrespective of the starting point. The phenomenon can be described thanks to the graphical description following the analysis given in [10] based on the least attenuated mode principle. While both modes have initially nearly the same (very low) decay, one of these mode becomes much more lossy after half of the encircling loop (loss is identified by the color map as shown). This is determined by the eigenvalue surface on which the mode is lying and therefore depends on the direction of encirclement. For instance, starting with the IP mode, it will remain on the least lossy surface in the CW direction whereas it will suffer from very strong attenuation

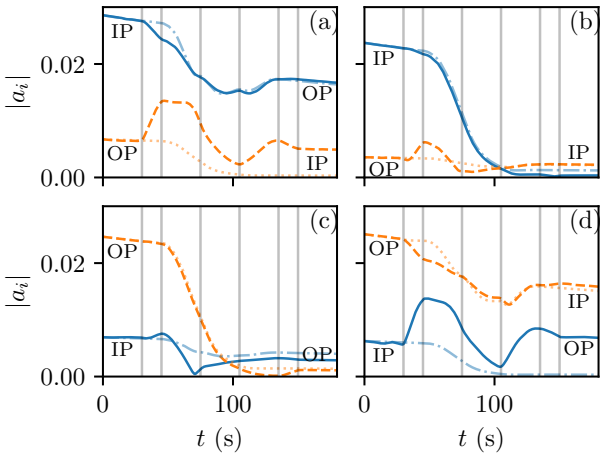

Figure 8. (color online) Modal coefficients starting mostly IP (blue solid line) and going (a) CW and (b) CCW, and starting mostly OP (orange dashed line) and going (c) CW and (d) CCW when $L_2(0) \approx L_2^0$.

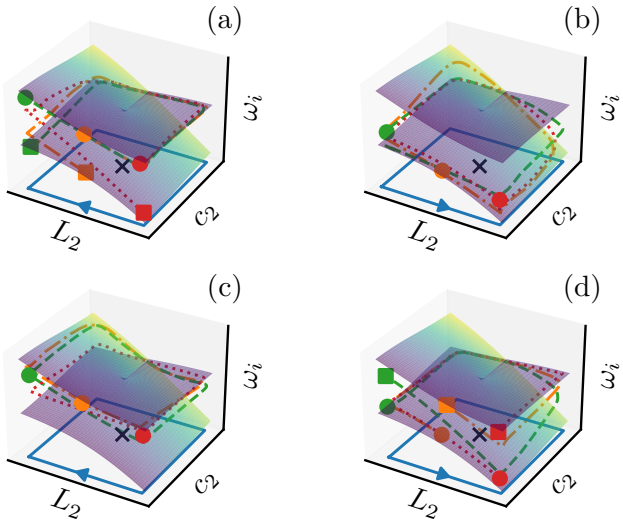

Figure 9. Trajectory of the averaged eigenvalue using a Riemann surface representation, (same legend as in Fig. 6). The first column corresponds to CW and the second to CCW encircling. The first row corresponds to an initially dominant IP state and the second to an initially dominant OP state. The green dashed, orange dash-dotted and red dotted lines stand for ($L_2^{\min}$, 0), (L_2^0, 0) and ($L_2^{\max}$, 0) starting points, respectively, indicated by a square marker, while the ending point is indicated by a circle. The period of encirclement is 120 s.

in the CCW direction. In this latter scenario, the other mode, initially small, becomes dominant after the loop due to the non-adiabatic coupling (see Fig. 8). The reader must be aware about the fact the trajectory of the averaged eigenvalue given by the ratio (4.4) masks the energy loss in the system, which is due to modal attenuation and also the period of encirclement. In this regard, we can refer to recent works like [23] which aim at optimizing the encirclement contour in order to minimize the loss.

For a more quantitative view, initial and final modal coefficient ratios are also provided in Table 3.

Table 3. White background $a_{\mathrm{IP}}/a_{\mathrm{OP}}$ and gray $a_{\mathrm{OP}}/a_{\mathrm{IP}}$. The associated contour are given in Fig. 4. The EP value is $c_2^0 \approx 0.12$.

Contour	Start		End	
	CW	CCW	CW	CCW
$L_2(0) = L_2^{\min}$	12.81	55.40	3.16	1.44
$c_2^{\max} \approx 0.19\,\mathrm{N\,m\,s}$	1.72	1.73	1.80	2.12
$L_2(0) = L_2^0$	4.20	6.90	3.41	7.56
$c_2^{\max} \approx 0.19\,\mathrm{N\,m\,s}$	3.47	4.22	2.69	2.35
$L_2(0) = L_2^{\max}$	2.74	2.31	2.95	1.83
$c_2^{\max} \approx 0.19\,\mathrm{N\,m\,s}$	4.20	3.37	2.36	2.96
$L_2(0) = L_2^0$	2.73	3.49	2.57	0.58
$c_2^{\max} \approx 0.07\,\mathrm{N\,m\,s}$	4.44	3.13	1.00	3.53

In a fourth scenario, we decided not to encircle the EP by following the rectangular contour (see Fig. 4) where $c_2^{\max} = 0.07$ with a period of encirclement of about 120 s. In this case, the chiral effect is not observed. The initial and final ratios, reported in the last line of Table 3, indicate a switch of the modal content, similar to Fig. 9(a) and (d), but in the other two cases (b) and (c), the final state contains the two modes with nearly the same magnitude. Furthermore, if the period is increased to 240 s, the switching phenomenon is less pronounced. Other experimental results have been carried out which tend to indicate that the transition between chiral or non-chiral regimes is rather progressive. In order to clarify this, a more systematic analysis is performed numerically in the next section.

6. Numerical observation of chiral behavior

In this last section, we shall take advantage of the numerical resolution of the dynamical system (2.2) in order to lead a parametric study illustrating both the effect of the period $T = 2\pi/\omega$ and the size of the contour which controls the amplitude of the controllable parameters. The contour, noted $\mathcal{E}(\epsilon, r)$, is chosen to be of elliptical shape as illustrated in Fig. 4 and parameters are given by

$$(L_2(t), c_2(t)) = (\bar{L}_2 - \epsilon \sin(\omega t),\ \bar{c}_2(\epsilon) - \epsilon r \cos(\omega t)), \tag{6.1}$$

where the center of the ellipse $\bar{L}_2,\ \bar{c}_2(\epsilon)$ are the averaged values. Here, $\bar{L}_2 = L_2^0$ and $\bar{c}_2$ depends on the size of the contour. Note that the elliptic path (6.1) is considered here as it serves to highlight in a simple manner the role of the period and the presence of the EP in the encirclement loop. It also makes the dynamical system (2.6) amenable to theoretical developments using the multiple-scale approach. Equations of motion are solved using the Runge-Kutta method for four independent initial conditions in order to construct the monodromy matrix $\boldsymbol{\Phi}$. This matrix is a matrix-valued function, whose columns are linearly independent solutions of the system of ODEs, evaluated after a single loop at $t = T$ see [16, Chap. 2.4]. The four independent solutions are obtained by fixing successively each degree of freedom of the initial state vector to one.

This allows one to write the state vector after a number n of encirclements:

$$\mathbf{p}(nT) = \boldsymbol{\Phi}^n \mathbf{p}(0). \tag{6.2}$$

Eigenvalues μ_i of the monodromy matrix are the Floquet multipliers, which inform us about periodic encircling.

In a first series of numerical tests, we consider the elliptical contour $\mathcal{E}(\epsilon = 0.036, r = 1.428)$ whose geometric proportion is identical to the rectangular contour used in our experiments. The modulus of the Floquet multipliers are plotted with respect to the period in Fig. 10. It is remarkable to see that the clockwise and counterclockwise scenarios are hardly distinguishable

and Floquet multipliers modulus are simply given by the eigenvalues of the averaged system, i.e. $\mu_i \approx \mathrm{e}^{\bar{\lambda}_i T}$. This changes noticeably when $T \approx 150\,\mathrm{s}$ and $T \approx 300\,\mathrm{s}$. In these situations, the monodromy matrix is nearly defective and the trajectory of the Floquet multipliers shares similarity with band gap or pitchfork bifurcation which is due to the existence of a branch point singularity (also called Floquet EP [14]) in the parametric ω-complex plane. Though this is not the place for a complete analysis, the distance to the singularity could be estimated by computing the condition number

$$\kappa(\mathbf{V}) = \|\mathbf{V}\|_2 \|\mathbf{V}^{-1}\|_2 \tag{6.3}$$

of the eigenvectors $\mathbf{V}$ of the monodromy matrix [43]. After several cycles, the Floquet mode having the highest eigenvalue is amplified giving rise to chirality and the system acts as a mode polarizer, as explained in [14]. In our example, chiral effects are expected to be more pronounced when the deviation from the time-averaged system is maximal and this happens when the amplitude of the driving frequency ω matches the difference between the two eigenvalues of the averaged system. This resonance condition is also discussed in [14] in the case of a complex-valued parametric modulation. If the amplitude of the perturbation is sufficiently small, i.e. $\epsilon \ll 1$ in Eq. (6.1), the resonance condition can be derived explicitly by application of the multiple-scale analysis (all details are given in App. A). The first resonances in the CW direction appear as a pair $(\pm)$ and

$$\omega^{\pm} = \bar{\omega}_2 - \bar{\omega}_1 \pm \epsilon\varsigma, \tag{6.4}$$

where $\bar{\omega}_i = -\mathrm{i}\bar{\lambda}_i$ and ς is defined in Eq. (A 14). This condition, which corresponds to a Floquet EP, signifies that the driving frequency must be necessarily complex-valued. If the parametric curve encircles or lies in the vicinity of an EP so that the two eigenvalues are nearly identical, $\bar{\omega}_1 \approx \bar{\omega}_2$, one can expect the period T to be large and nearly real-valued for small values of ϵ. In the lossless case, i.e. $\epsilon = 0$, we can calculate that $T = 2\pi(\bar{\omega}_2 - \bar{\omega}_1)^{-1} \approx 150\mathrm{s}$. Results in Fig. 10 show a resonance effect around $T \approx 150$ s which corresponds to roughly 75 pendulums oscillations (the second resonance which appears at approximately $2T$ stems from the quadratic term in (A 1) is not described in the theoretical analysis given in Appendix). This example shows that chirality can be observed even though EP is not encircled [14].

In a second series of numerical tests, we consider the elliptical contour $\mathcal{E}(\epsilon = 0.0604, r = 1.428)$ which now encircles the exceptional point (the limit case corresponds to $\epsilon = 0.043$). Again, the clockwise and counterclockwise scenarios are hardly indistinguishable until the encirclement period is sufficiently large. Indeed, as soon as $T \geq 150$ s, the departure from the averaged values can be observed. A closer analysis reveals that this is the result of the merging of the two resonance regions which grows with ϵ.

This is well illustrated in Fig. 11 where the condition number of the eigenvectors of the monodromy matrix is plotted for a large set of values for the period T and the contour size ϵ. Comparison between the clockwise and counterclockwise encirclement show very similar results, although CCW shows more contrast. When there is no encirclement, i.e. when $\epsilon \leq 0.043$, one clearly distinguishes the two resonance regions. The first one fits perfectly with Eq. (6.4) and confirms the validity of the multiple scale approach, at least when ϵ is sufficiently small. Above this value, the resonance regions merge, they can not be distinguished any more. This gives rise to a region identified by a large condition number. This reflects non-normal dynamics [44] where non Hermitian effects are present and where conditions for achieving chirality are most favourable.

In order to establish a link with chirality in conjunction with our experiments, the same exhaustive study is carried out. In each case, a pure mode, either IP or OP, is initially imposed. After a single clockwise or counterclockwise loop, the ratios of amplitudes are plotted in Fig. 12(a). Each of the 4 figures can be viewed as a generalisation, via numerical simulation, of the experimental results of Fig. 9. Clearly, strong chirality effects are observed if the EP lies in the contour and if the encirclement period is above the first resonance period. In these conditions, a CW encirclement leads to a dominant OP mode whereas a CCW one leads to a dominant IP one irrespective of the initial mode. Conversion ratio are in line with experimental results (even though for the latter, initial states are a combination of IP and OP modes).

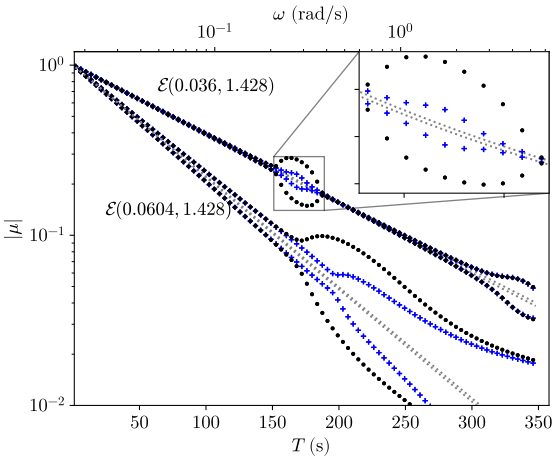

Figure 10. (color online) Modulus of the Floquet multipliers for $\mathcal{E}(0.036, 1.428)$ and $\mathcal{E}(0.060, 1.428)$ contours for both orientations. The markers $+$ and $\cdot$ stand for CW and CCW encircling, respectively. The two dotted gray lines indicate the Floquet multipliers for the averaged system.

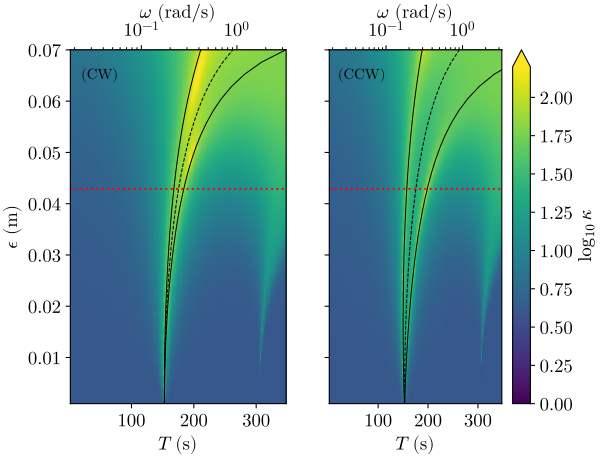

Figure 11. Condition number of the eigenvectors of the monodromy matrix for CW (left) or CCW (right) encirclement. Resonances condition (6.4) are also indicated in black.

When the number of cycle increases, the chiral zone is a little modified as shown by the iso-contours in Fig. 12(b), which tend to be aligned with the resonance regions. The identification of the chiral zone is in line with the previous observation made earlier on the conditioning number of Fig. 11 and this shows that the study of the monodromy matrix provides useful information on the periodic encircling. The authors are aware that the analysis given above should serve as a guideline and a more thorough analysis could be carried out by analyzing, for instance, the content of the Floquet modes with respect to the initial OP/IP modes or by considering a different initial state. Further investigation could also be pursued in order to consider other type of contour such as the rectangular one used in our experiment (this has been shown to deliver a similar trend) and/or different time history curves for the parameters.

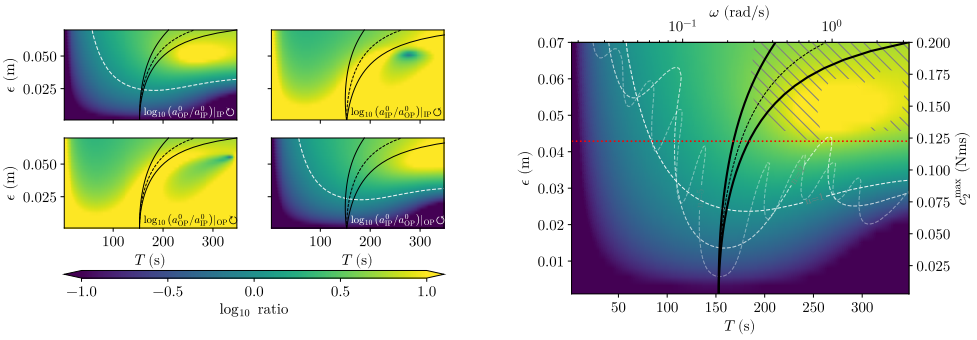

Figure 12. Ratio of the modal amplitudes after a single clockwise or counterclockwise loop. In all cases, a pure mode, either IP or OP, is initially imposed. Resonances (6.4) are also indicated in black. In the magnified view (b) of the first scenario (top left) iso-contours corresponding to a ratio equal to 1 are also shown for 1, 2 and 5 loops. The EP is encircled if $\epsilon > 0.043$ (indicated by the red dotted line). Modal ratio above 3 are identified by the hatch area (recall that chiral regions are identified in yellow colour).

7. Conclusion

In this work, the dynamical encirclement of an exceptional point (EP) is demonstrated experimentally in the case of a simple vibration system consisting of two linearized coupled pendulums. This simple system can be considered as a toy model which mimics numerous applications encountered in physics. It also brings to light the interdisciplinary significance of EPs, and in particular, their importance in mechanical vibration where energy mitigation, harvesting [20] and transfer between oscillators are of primary interest.

The experimental device has been designed with two time-dependent controllable parameters which are the length of one pendulum and a viscous-like damping which is produced via electromagnetic induction. What distinguishes the present work from most studies is the fact that controllable parameters are real-valued. The device allows for easy control of the encircling loop, including control of the encircling direction and the shape of the enclosing paths. Experimental data, which are the angular displacements, are processed using a extended Kalman filter algorithm which allows one to retrieve all time-dependent variables, i.e. angular displacements and controllable parameters, as well as their first derivatives. The algorithm developed is well adapted for EP based application due to the high sensitivity in the vicinity of the EP which requires accurate identification and tuning.

The evolution of the dynamical system is described via the analysis of the modal coefficients. By assuming that parameters are slowly-varying, it is shown that modal amplitudes can be expressed explicitly as a the sum of an adiabatic solution and a coupling term which is responsible for mode energy transfer. In all situations considered in this paper, the initial state is lossless, either in-phase (IP), out-of-phase (OP) or a combination of both. After a single loop, our experimental results showed that the initially dominant mode evolves adiabatically and undergoes an interchange of mode, the so-called “state-flip”, which is a consequence of the presence of an EP inside the parametric loop. The other mode exhibits, via mode coupling mechanisms, sharp variations in response to the variations of the controllable parameters.

The analysis of the trajectory of the averaged eigenvalue (4.4) allows us to observe chiral transformations whereby the dominant state, after a single loop, depends solely on the direction of encirclement. Another series of experiments have been carried out in order to identify both the effect of the presence (or not) of an EP in the loop and the period of encirclement. It is concluded that the transition between chiral or non-chiral regimes is rather progressive.

The paper finishes with a parametric study, using numerical simulations, in order to illustrate both the effect of the encircling time and the size of the contour. It turns out that conditions for strong chirality are met as long as the EP lies in the contour and if the encirclement period is sufficiently large, i.e. above a resonance period associated with a driving frequency which matches the difference between the two eigenvalues of the averaged system. In this regard, it also shown that the eigendecomposition of the monodromy matrix, accessible either from experiment or via numerical computation, can provide an interesting analysis tool.

Data Accessibility. The data are available on zenodo: https://zenodo.org/records/15299253 see details in [45]

A. Multiple scale method

In this section, we apply the multiple-scale approach, originally developed in the lossless case in Nayfeh's textbook [46, Chap. 5], to the original matrix system written in its state-space form (2.6). Here, it is assumed that the varying parameters describe the elliptical contour (6.1) either in the CW ($\omega \geq 0$) or CCW direction ($\omega \leq 0$). The system is rewritten as a power series as

$$(\mathbf{A}_0 + \epsilon \mathbf{A}_1)\,\mathbf{p} = \left(\mathbf{B}_0 + \epsilon \mathbf{B}_1 + \epsilon^2 \mathbf{B}_2\right)\dot{\mathbf{p}} \tag{A 1}$$

where matrices $\mathbf{A}_i$ and $\mathbf{B}_i$ derive from the original matrices after substituting (6.1).

Standard perturbation theory yields growing terms (in time), also called secular terms. They arise because the zeroth-order solution acts as a forcing function for the correction terms and this gives rise to resonance. In order to remove secular terms, the method of multiple scales is generally applied [46]. This starts by defining the two time scales: $\xi = t$ and $\eta = \epsilon t$ so the time derivative formula becomes

$$\frac{\partial}{\partial t} \equiv \frac{\partial}{\partial \xi} + \epsilon \frac{\partial}{\partial \eta}. \tag{A 2}$$

The first step is to seek the solution in the *averaged* eigenmode basis (identified by the bar symbol) as

$$\mathbf{p} = \sum_{i=1}^{4} a_i \bar{\mathbf{x}}_i = \bar{\mathbf{X}}\mathbf{a} \tag{A 3}$$

where it is assumed that the modal coordinates can be expressed as the perturbation series

$$\mathbf{a} = \mathbf{a}_0(\xi, \eta) + \epsilon \mathbf{a}_1(\xi, \eta) + \cdots. \tag{A 4}$$

After using (A 2), and applying standard bi-orthogonality relations, we end up with a series of equations (we only write the leading order and the first order correction):

$$\bar{\Lambda}\mathbf{a}_0 - \frac{\partial \mathbf{a}_0}{\partial \xi} = \mathbf{0}, \tag{A 5a}$$

$$\bar{\Lambda}\mathbf{a}_1 - \frac{\partial \mathbf{a}_1}{\partial \xi} = \frac{\partial \mathbf{a}_0}{\partial \eta} + \bar{\mathbf{Y}}^{\mathrm{H}}\mathbf{B}_1\bar{\mathbf{X}}\frac{\partial \mathbf{a}_0}{\partial \xi} - \bar{\mathbf{Y}}^{\mathrm{H}}\mathbf{A}_1\bar{\mathbf{X}}\mathbf{a}_0, \tag{A 5b}$$

where the diagonal matrix $\bar{\Lambda}$ contains the averaged eigenvalues: $\bar{\lambda}_i = \mathrm{i}\bar{\omega}_i$. The general solution of (A 5*a*) is

$$\mathbf{a}_0(\xi, \eta) = \mathrm{e}^{\bar{\Lambda}\xi}\boldsymbol{\alpha}(\eta), \tag{A 6}$$

where the modal amplitude vector $\boldsymbol{\alpha}(\eta)$ is function of the slow variable. Eigenvalues are ordered as follows $\bar{\Lambda} = \mathrm{diag}(\bar{\lambda}_1, \bar{\lambda}_1^*, \bar{\lambda}_2, \bar{\lambda}_2^*)$ and similarly $\boldsymbol{\alpha} = [\alpha_1, \alpha_1^*, \alpha_2, \alpha_2^*]^{\mathrm{T}}$ to be consistent

with sec. 4(b). The RHS terms in (A 5*b*) read explicitly

$$\begin{aligned}\bar{\mathbf{Y}}^{\mathrm{H}}\mathbf{A}_1\mathbf{X} &= \bar{\mathbf{Y}}^{\mathrm{H}}\mathbf{A}_1^{\mathbf{K}}(\xi)\bar{\mathbf{X}} + \bar{\mathbf{Y}}^{\mathrm{H}}\mathbf{A}_1^{\mathbf{C}}(\xi)\bar{\mathbf{X}}\\ &= \mathbf{G}^{\mathbf{K}}\sin(\omega\xi) + \mathbf{G}^{\mathbf{C}}\cos(\omega\xi)\\ \bar{\mathbf{Y}}^{\mathrm{H}}\mathbf{B}_1\bar{\mathbf{X}} &= \mathbf{G}^{\mathbf{M}}\sin(\omega\xi)\end{aligned} \tag{A 7}$$

where superscripts $^{\mathbf{M},\mathbf{C},\mathbf{K}}$ have been added in order to identify which part of the matrix system (2.2) they originate from. We end up with the system of coupled equation for the first order correction:

$$\begin{aligned}\mathrm{i}\bar{\omega}_i a_{1,i} - \frac{\partial a_{1,i}}{\partial\xi} &= \mathrm{e}^{\mathrm{i}\bar{\omega}_i\xi}\frac{\partial\alpha_i}{\partial\eta}\\ &+ \frac{1}{2}\left(G^{+}_{i1}\mathrm{e}^{\mathrm{i}(\bar{\omega}_1+\omega)\xi} + G^{-}_{i1}\mathrm{e}^{\mathrm{i}(\bar{\omega}_1-\omega)\xi}\right)\alpha_1\\ &+ \frac{1}{2}\left(G^{+}_{i3}\mathrm{e}^{\mathrm{i}(\bar{\omega}_2+\omega)\xi} + G^{-}_{i3}\mathrm{e}^{\mathrm{i}(\bar{\omega}_2-\omega)\xi}\right)\alpha_2 + \ldots\end{aligned} \tag{A 8}$$

where

$$G^{\pm}_{i1} = \pm\mathrm{i}G^{\mathbf{K}}_{i1} - G^{\mathbf{C}}_{i1} \pm \bar{\omega}_1 G^{\mathbf{M}}_{i1}, \tag{A 9a}$$

$$G^{\pm}_{i3} = \pm\mathrm{i}G^{\mathbf{K}}_{i3} - G^{\mathbf{C}}_{i3} \pm \bar{\omega}_2 G^{\mathbf{M}}_{i3}. \tag{A 9b}$$

In order to remove the secular terms we put

$$\omega = \bar{\omega}_2 - \bar{\omega}_1 + \epsilon\varsigma, \tag{A 10}$$

and solve the 2×2 coupled system

$$\frac{\partial\alpha_1}{\partial\eta} + \frac{1}{2}G^{-}_{13}\mathrm{e}^{-\mathrm{i}\varsigma\eta}\alpha_2 = 0, \tag{A 11a}$$

$$\frac{\partial\alpha_2}{\partial\eta} + \frac{1}{2}G^{+}_{31}\mathrm{e}^{\mathrm{i}\varsigma\eta}\alpha_1 = 0. \tag{A 11b}$$

This yields the family of solutions

$$\alpha_1(\eta) = \alpha_1^{+}\mathrm{e}^{\lambda^{+}\eta} + \alpha_1^{-}\mathrm{e}^{\lambda^{-}\eta}, \tag{A 12a}$$

$$\alpha_2(\eta) = \alpha_2^{+}\mathrm{e}^{-\lambda^{+}\eta} + \alpha_2^{-}\mathrm{e}^{-\lambda^{-}\eta} \tag{A 12b}$$

where $\alpha_i^{\pm}$ are arbitrary constants and

$$\lambda^{\pm} = -\frac{1}{2}\mathrm{i}\left(\varsigma \pm \sqrt{\varsigma^2 - G^{-}_{13}G^{+}_{31}}\right). \tag{A 13}$$

It follows that the particular choice

$$\varsigma^2 = G^{-}_{13}G^{+}_{31} \tag{A 14}$$

yields a double root which corresponds to a Floquet EP. In other words, if we allow ω to be complex-valued satisfying the resonance condition

$$\omega = \bar{\omega}_2 - \bar{\omega}_1 \pm \epsilon\sqrt{G^{-}_{13}G^{+}_{31}}, \tag{A 15}$$

the monodromy matrix becomes defective. Note that condition (A 15) corresponds to a CW encirclement, i.e. the real part of ω is positive and a similar approach can be followed for the CCW encirclement involving $-\bar{\omega}_1^{*}$ and $-\bar{\omega}_2^{*}$. A validation using direct computation of condition number of the eigenvector of the monodromy matrix is given in Fig. 11.

Matrices involved in (A 7) (remind that right eigenvectors have the general form $\bar{\mathbf{x}} = [\bar{v}, \bar{\lambda}\bar{v}]^{\mathrm{T}}$[2]) read:

$$\mathbf{G}^{\mathbf{K}}_{ij} = (\bar{\mathbf{y}}^{*}_{4,i}\bar{\mathbf{x}}_{2,j})m_2 g, \tag{A 16}$$

$$\mathbf{G}^{\mathbf{C}}_{ij} = (\bar{\mathbf{y}}^{*}_{4,i}\bar{\mathbf{x}}_{4,j})r = \bar{\lambda}_j(\mathbf{y}^{*}_{4,i}\bar{\mathbf{x}}_{2,j})r, \tag{A 17}$$

$$\mathbf{G}^{\mathbf{M}}_{ij} = -(\bar{\mathbf{y}}^{*}_{4,i}\bar{\mathbf{x}}_{4,j})2m_2\bar{L}_2 = -\bar{\lambda}_j(\bar{\mathbf{y}}^{*}_{4,i}\bar{\mathbf{x}}_{2,j})2m_2\bar{L}_2. \tag{A 18}$$

It needs to be pointed out that the slope ς is very sensitive to the ellipse aspect ratio r. Using Eqs. (A 16), the CW slope can written as

$$\varsigma^2 = \chi_{13}\underbrace{\left(\mathrm{i}m_2 g + \bar{\lambda}_2 r + 2\mathrm{i}\bar{\lambda}_2^2 m_2\bar{L}_2\right)\left(\mathrm{i}m_2 g - \bar{\lambda}_1 r + 2\mathrm{i}\bar{\lambda}_1^2 m_2\bar{L}_2\right)}_{\Theta} \tag{A 19}$$

where $\chi_{13} = -(\bar{\mathbf{y}}^{*}_{4,1}\bar{\mathbf{x}}_{2,1})(\bar{\mathbf{y}}^{*}_{4,3}\bar{\mathbf{x}}_{2,3})$.

For the configurations considered in this work, numerical tests have shown that χ_{13} is a positive real number with negligible imaginary part. Similarly, averaged eigenvalues $\bar{\lambda}_i$ have a very small real part so the term Θ is nearly real-valued. It vanishes for the critical value

$$r_c = -\mathrm{i}m_2\left(g + 2\bar{L}_2\bar{\lambda}_2^2\right)/\bar{\lambda}_2. \tag{A 20}$$

The critical value associated with our experiment is nearly real-valued (and positive) with $r_c \approx 1.43 + 0.001\mathrm{i} \approx 1.43$ and $r_c = 1.34$ for CW and CCW orientation respectively. Thus, when $r < r_c$, ς is almost an imaginary number which signifies that the resonance condition (A 15) is only satisfied if the encirclement period is complex-valued. On the other hand, if $r > r_c$, the resonance frequency is nearly real-valued and can therefore be observed in practice. It needs to be pointed out that the theory becomes relevant for a sufficient number of encirclements and for a single loop the resonance effect is less pronounced.

References

1. Tosio Kato.
   Perturbation Theory for Linear Operators.
   Springer, 1966.
2. Nimrod Moiseyev.
   Non-Hermitian Quantum Mechanics.
   Cambridge University Press, 2011.
3. W. D. Heiss.
   The physics of exceptional points.
   Journal of Physics A: Mathematical and Theoretical, 45:444016, 2012.
4. Mohammad-Ali Miri and Andrea Alù.
   Exceptional points in optics and photonics.
   Science, 363:eaar7709, 2019.
5. Carl M Bender, Patrick E Dorey, Clare Dunning, Andreas Fring, Daniel W Hook, Hugh F Jones, Sergii Kuzhel, Géza Lévai, and Roberto Tateo.
   PT Symmetry: In Quantum and Classical Physics.
   WORLD SCIENTIFIC (EUROPE), 2019.
6. W. D. Heiss.
   Repulsion of resonance states and exceptional points.
   Physical Review E, 61:929–932, 2000.
7. Michael Victor Berry.
   Quantal phase factors accompanying adiabatic changes.
   Proceedings of the Royal Society of London. A. Mathematical and Physical Sciences, 392:45–57, 1984.
8. C. Dembowski, H.-D. Gräf, H. L. Harney, A. Heine, W. D. Heiss, H. Rehfeld, and A. Richter.
   Experimental Observation of the Topological Structure of Exceptional Points.
   Physical Review Letters, 86:787–790, 2001.

[2]This relation also holds for the left eigenvector $\mathbf{y}$ if another linearization is used, see [37, Eq. (3.6)]

9. T. Gao, E. Estrecho, K. Y. Bliokh, T. C. H. Liew, M. D. Fraser, S. Brodbeck, M. Kamp, C. Schneider, S. Höfling, Y. Yamamoto, F. Nori, Y. S. Kivshar, A. G. Truscott, R. G. Dall, and E. A. Ostrovskaya.
Observation of non-Hermitian degeneracies in a chaotic exciton-polariton billiard.
Nature, 526:554–558, 2015.
10. Raam Uzdin, Alexei Mailybaev, and Nimrod Moiseyev.
On the observability and asymmetry of adiabatic state flips generated by exceptional points.
Journal of Physics A: Mathematical and Theoretical, 44:435302, 2011.
11. M. V. Berry and R. Uzdin.
Slow non-Hermitian cycling: Exact solutions and the Stokes phenomenon.
Journal of Physics A: Mathematical and Theoretical, 44:435303, 2011.
12. S. Ibáñez and J. G. Muga.
Adiabaticity condition for non-Hermitian Hamiltonians.
Physical Review A, 89:033403, 2014.
13. Thomas J. Milburn, Jörg Doppler, Catherine A. Holmes, Stefano Portolan, Stefan Rotter, and Peter Rabl.
General description of quasiadiabatic dynamical phenomena near exceptional points.
Physical Review A, 92:052124, 2015.
14. Stefano Longhi.
Floquet exceptional points and chirality in non-Hermitian Hamiltonians.
Journal of Physics A: Mathematical and Theoretical, 50:505201, 2017.
15. Aleksi Bossart and Romain Fleury.
Non-Hermitian time evolution: From static to parametric instability.
Physical Review A, 104:042225, 2021.
16. Carmen Chicone.
Ordinary Differential Equations with Applications, volume 34.
Springer New York, 2006.
17. Jörg Doppler, Alexei A. Mailybaev, Julian Böhm, Ulrich Kuhl, Adrian Girschik, Florian Libisch, Thomas J. Milburn, Peter Rabl, Nimrod Moiseyev, and Stefan Rotter.
Dynamically encircling an exceptional point for asymmetric mode switching.
Nature, 537:76–79, 2016.
18. Xu-Lin Zhang, Shubo Wang, Bo Hou, and C. T. Chan.
Dynamically Encircling Exceptional Points: In situ Control of Encircling Loops and the Role of the Starting Point.
Physical Review X, 8:021066, 2018.
19. Xu-Lin Zhang, Tianshu Jiang, and C. T. Chan.
Dynamically encircling an exceptional point in anti-parity-time symmetric systems: Asymmetric mode switching for symmetry-broken modes.
Light: Science & Applications, 8:88, 2019.
20. H. Xu, D. Mason, Luyao Jiang, and J. G. E. Harris.
Topological energy transfer in an optomechanical system with exceptional points.
Nature, 537:80–83, 2016.
21. Jae Woong Yoon, Youngsun Choi, Choloong Hahn, Gunpyo Kim, Seok Ho Song, Ki-Yeon Yang, Jeong Yub Lee, Yongsung Kim, Chang Seung Lee, Jai Kwang Shin, Hong-Seok Lee, and Pierre Berini.
Time-asymmetric loop around an exceptional point over the full optical communications band.
Nature, 562:86–90, 2018.
22. Weiwei Liu, Yicong Zhang, Zhihua Deng, Jianghua Ye, Kai Wang, Bing Wang, Dingshan Gao, and Peixiang Lu.
On-Chip Chiral Mode Switching by Encircling an Exceptional Point in an Anti-Parity-Time Symmetric System.
Laser & Photonics Reviews, 16:2100675, 2022.
23. Xiaoqian Shu, Aodong Li, Guangwei Hu, Jian Wang, Andrea Alù, and Lin Chen.
Fast encirclement of an exceptional point for highly efficient and compact chiral mode converters.
Nature Communications, 13:2123, 2022.
24. M. Said Ergoktas, Sina Soleymani, Nurbek Kakenov, Kaiyuan Wang, Thomas B. Smith,

Gokhan Bakan, Sinan Balci, Alessandro Principi, Kostya S. Novoselov, Sahin K. Ozdemir, and Coskun Kocabas.
Topological engineering of terahertz light using electrically tunable exceptional point singularities.
Science, 376:184–188, 2022.

25. Arnab Laha, Abhijit Biswas, and Somnath Ghosh.
Nonadiabatic Modal Dynamics Around Exceptional Points in an All-Lossy Dual-Mode Optical Waveguide: Toward Chirality-Driven Asymmetric Mode Conversion.
Physical Review Applied, 10:054008, 2018.
26. Absar U. Hassan, Bo Zhen, Marin Soljačić, Mercedeh Khajavikhan, and Demetrios N. Christodoulides.
Dynamically Encircling Exceptional Points: Exact Evolution and Polarization State Conversion.
Physical Review Letters, 118:093002, 2017.
27. Lei Xiong, Benoit Nennig, Yves Aurégan, and Wenping Bi.
Sound attenuation optimization using metaporous materials tuned on exceptional points.
The Journal of the Acoustical Society of America, 142:2288–2297, 2017.
28. E. Perrey-Debain, B. Nennig, and J.B. Lawrie.
Mode coalescence and the green's function in a two-dimensional waveguide with arbitrary admittance boundary conditions.
Journal of Sound and Vibration, page 116510, 2021.
29. Jane B. Lawrie, B. Nennig, and E. Perrey-Debain.
Analytic mode-matching for accurate handling of exceptional points in a lined acoustic waveguide.
Proceedings of the Royal Society A: Mathematical, Physical and Engineering Sciences, 478:20220484, 2022.
30. Xu-Lin Zhang, Jun-Feng Song, C. T. Chan, and Hong-Bo Sun.
Distinct outcomes by dynamically encircling an exceptional point along homotopic loops.
Physical Review A, 99:063831, 2019.
31. Absar U. Hassan, Gisela L. Galmiche, Gal Harari, Patrick LiKamWa, Mercedeh Khajavikhan, Mordechai Segev, and Demetrios N. Christodoulides.
Chiral state conversion without encircling an exceptional point.
Physical Review A, 96:052129, 2017.
32. Absar U. Hassan, Gisela L. Galmiche, Gal Harari, Patrick LiKamWa, Mercedeh Khajavikhan, Mordechai Segev, and Demetrios N. Christodoulides.
Erratum: Chiral state conversion without encircling an exceptional point [Phys. Rev. A 96, 052129 (2017)].
Physical Review A, 96:069908(E), 2017.
33. Youdong Duan, Linlin Geng, Qiuquan Guo, Jun Yang, Gengkai Hu, and Xiaoming Zhou.
Acoustic chiral mode switching by dynamic encircling of exceptional points.
Applied Physics Letters, 123(10):101701, 2023.
34. Linlin Geng, Weixuan Zhang, Xiangdong Zhang, and Xiaoming Zhou.
Topological mode switching in modulated structures with dynamic encircling of an exceptional point.
Proceedings of the Royal Society A: Mathematical, Physical and Engineering Sciences, 477:20200766, 2021.
35. N. Even, B. Nennig, G. Lefebvre, and E. Perrey-Debain.
Experimental observation of exceptional points in coupled pendulums.
Journal of Sound and Vibration, 575:118239, 2024.
36. Roger Labbe.
Kalman and Bayesian Filters in Python.
https://github.com/rlabbe/Kalman-and-Bayesian-Filters-in-Python, 2014.
37. Françoise Tisseur and Karl Meerbergen.
The Quadratic Eigenvalue Problem.
SIAM Review, 43:235–286, 2001.
38. H. A. Haus and W. Huang.
Coupled-mode theory.
Proceedings of the IEEE, 79(10):1505–1518, 1991.

39. Alan L. Andrew, K.-W. Eric Chu, and Peter Lancaster.
Derivatives of Eigenvalues and Eigenvectors of Matrix Functions.
SIAM Journal on Matrix Analysis and Applications, 14:903–926, 1993.
40. Alexei A. Mailybaev, Oleg N. Kirillov, and Alexander P. Seyranian.
Geometric phase around exceptional points.
Physical Review A, 72:014104, 2005.
41. R. Roy, A. Paulraj, and T. Kailath.
ESPRIT–A subspace rotation approach to estimation of parameters of cisoids in noise.
IEEE Transactions on Acoustics, Speech, and Signal Processing, 34:1340–1342, 1986.
42. H. E. Rauch, F. Tung, and C. T. Striebel.
Maximum likelihood estimates of linear dynamic systems.
AIAA Journal, 3:1445–1450, 1965.
43. Sk Ahmad and Rafikul Alam.
On wilkinson's problem for matrix pencils.
The Electronic Journal of Linear Algebra, 30:632–648, 2015.
44. Lloyd N. Trefethen and Mark Embree.
Spectra and Pseudospectra: The Behavior of Nonnormal Matrices and Operators.
Princeton University Press, 2005.
45. Nicolas Even, Benoit Nennig, Gautier Lefebvre, and Emmanuel Perrey-Debain.
Data used in "experimental dynamical encircling of an exceptional point in coupled pendulums", April 2025.
46. Ali H. Nayfeh and Dean T. Mook.
Nonlinear Oscillations.
John Wiley & Sons, 2008.